

Impacts of grid turbulence on the side projection of planar shock waves

Gaku Fukushima, Shingo Ogawa, Jiaxi Wei, Yusuke Nakamura, and Akihiro Sasoh

Key words: Shock wave modulation, turbulence, shock-turbulence interaction

Abstract

In this study, the characteristics of side-projected planar shock waves propagating through grid turbulence were investigated using a counter-driver shock tube. At the location of visualization of the shock–turbulence interactions, the range of the shock Mach number was $M_s = 1.01$ – 1.15 , and the representative value of the turbulent Mach number was $\widetilde{M}_t = 0.005$ – 0.014 . The interaction length between the shock wave and grid turbulence was in the range of approximately from -50 to 300 times the integral length scale of the turbulence. For the interaction involving the strongest turbulence with $\widetilde{M}_t = 0.014$, the weakest planar shock wave with $M_s = 1.01$ could not be detected on the projected shadowgraph and schlieren images. The density changes on the grayscale in the projected images of the shock waves weakened and expanded multidimensionally. This undetectable profile of the shock wave could indicate that the shock wave locally lost discontinuous properties change profile. The shock waves with $M_s > 1.05$ did not show the undetectable profile in the projected image. In these cases, the projected thickness of the shock wave increased with an increase in the interaction length. The increase in the projected thickness became larger as the turbulent Mach number increased, and the shock Mach number decreased.

1. Introduction

A shock–turbulence interaction is a mutual phenomenon involving the complex modulation of shock waves and turbulence [\[1\]](#). Changes in the strength of a shock wave owing to velocity fluctuations in the path of shock propagation are commonly known as shock wave modulations [\[2, 3\]](#). The shock wave becomes stronger if an opposing flow exists in the direction of the shock wave propagation. In contrast, if the velocity field is in the same direction as the traveling direction of the shock wave, the shock wave becomes weaker. These shock wave modulations are closely related to the sonic boom generated by a supersonic flight. Research on the ground measurement of a sonic boom indicates that the pressure history varies greatly depending on the measurement position because the intensity of the shock wave is modulated by atmospheric turbulence. In some cases, the pressure behind the shock wave increases, and the rise time of the pressure decreases. In other cases, the shock wave is weakened; thus, the pressure rise becomes small, and the rise time of the pressure becomes long [\[4\]](#). A fundamental understanding of shock–turbulence interactions from the perspective of fluid physics is needed to clarify these pressure modulation characteristics behind shock waves and facilitate quantitative predictions. In practical situations, such as sonic boom modulation, the effects of the shock Mach number (a value obtained by dividing the relative velocity of the shock wave to the flow in front of the shock wave by the sound velocity in the gas in front of the shock wave) and turbulent Mach number (a value obtained by dividing the root-mean-square value of velocity fluctuation of turbulence by the sound velocity in the turbulence) should be evaluated. In addition, the effect of the propagation length through the turbulent field on the shock wave should be investigated.

When investigating the interaction between shock waves and turbulence, the following two types of

boundary conditions are typically considered depending on whether the shock wave is fixed or propagates in space. In the first case, the region upstream of the shock wave is a steadily turbulent field where the average Mach number is constant. In this case, if the ensemble average of the Mach number of the upstream flow is constant, the interacting shock wave and the corresponding region will settle into a steady state even when there are some fluctuations in the upstream flow. Some of the previous experiments [¥cite{Ref5,Ref6}](#) and most of the previous numerical analyses [¥cite{Ref7}](#)-[¥cite{Ref13}](#) have used such boundary condition settings. In this case, the main point of interest is the phenomena in the steady state. For such conditions, numerous results have been obtained by direct numerical simulations [¥cite{Ref7,Ref8,Ref9,Ref,10,Ref11,Ref12,Ref13,Ref14}](#). Shock waves have the following impact on turbulence: turbulent velocity fluctuations are amplified, and the scales of turbulence are reduced because of instantaneous compression by the shock waves. The effect of the Mach number and Reynolds number on the amplification of velocity fluctuations has been investigated [¥cite{Ref13,Ref15}](#). In addition, some studies have investigated the effect of turbulence on shock waves. A shock wave undergoes considerable deformation when the turbulence is relatively strong against the shock wave, and the density increase owing to the shock wave varies greatly. Past numerical studies have proposed shock wave profiles with the following three states: the “wrinkled” state, where deformations occur on the shock wave; the “broken” state, where local holes appear on the shock wave, and a gradual change in quantities is observed before and after the shock wave; and the “vanished” state, where the shock wave disappears entirely [¥cite{Ref15}](#). The broken state appears depending on the relationship between the mean Mach number M of the region upstream of the shock wave and the turbulent Mach number M_t . The inequalities $M_t^2 \geq 0.1 (M^2 - 1)$

ζ [Ref7] and $M_t^2 \geq 0.06 (M^2 - 1)$ [Ref8] are obtained from direct numerical simulation (DNS) results, and the inequality $M_t \geq 0.6 (M - 1)$ [Ref9,Ref13,Ref16] is obtained from theoretical analysis and DNS results. However, in such numerical calculations, the shock wave intensity is fixed by applying a boundary condition based on the Rankine–Hugoniot equation [Ref17] involving the turbulence effect. Therefore, it is not clear whether unsteadily propagating shock waves follow the criteria obtained by these numerical calculations.

For the second type of boundary condition, the shock wave unsteadily propagates in space and passes through the turbulent field. For example, when a supersonic airplane steadily flies in a static field, shock waves with a spatial distribution are propagated, as observed from a coordinate fixed on the ground. In this case, when the shock wave interacts with turbulence, the properties of the shock wave, including the shock Mach number M_s , change mainly because of the velocity fluctuations of the turbulence. To generate shock waves propagating in space, electric discharge, laser-induced breakdown [Ref18,Ref19], explosives [Ref20], and an open-end shock tube [Ref21,Ref22,Ref23,Ref24] have been used in previous studies. However, the shock waves generated by these methods are referred to as a “blast wave” with an expansion region immediately behind the shock wave. Then, as the shock wave propagates, the overpressure and M_s of the shock wave decrease. An effective method to investigate the unsteady effects of turbulence on the shock waves propagating in space is to examine a simple system in which the properties of the shock waves do not change during their propagation. In contrast to these blast wave generation methods, a shock tube can generate a planar shock wave whose one-dimensional properties do not change depending on the distance. Previous studies have performed shock–

turbulence interaction experiments using a shock tube [\[Ref25,Ref26,Ref27,Ref28,Ref29\]](#). However, these studies could not independently control the turbulence Mach number and interaction length for a given M_s because of the limitations of the experimental facilities. To overcome these limitations, Tamba et al. [\[Ref30\]](#) developed a counter-driver shock tube (CD-ST), which facilitated the use of a wide range of M_s , M_t , and interaction length values. In our previous study [\[Ref31\]](#), only results for a fixed shock Mach number ($M_s = 1.03\text{--}1.05$) were obtained. Hence, further experiments are required to obtain general information about shock–turbulence interactions.

As an extension of our previous study [\[Ref31\]](#), in this study, we experimentally investigated the interaction of the planar shock wave in the range of $M_s = 1.01\text{--}1.15$ with grid turbulences of $M_t = 0.005, 0.009,$ and 0.014 using the CD-ST. In addition, we varied the interaction length of the shock wave with the grid turbulence under each set of M_s and M_t values. From optically visualized side-view images of the shock wave propagating in the turbulent field, the effects of the shock Mach number, turbulent Mach number, and interaction length on the projected thickness and profile of the projected image of the shock wave were evaluated.

2. Experimental setup

In the experiment, we used a CD-ST, which had a driver on the left- and right-hand sides of the driven section and a cross section of $120\text{ mm} \times 120\text{ mm}$. Our previous papers provide details about the working principle of the CD-ST [\[Ref30\]](#) and the detailed setup for the interaction between a planar shock wave and grid turbulence [\[Ref31\]](#). In this study, the shock tube length was increased by 4 m compared to that in the

previous study [cite{Ref31}](#), and the total length of the CD-ST was approximately 14 m. In addition, new devices were added to facilitate wide variations in the shock Mach number and turbulent Mach number, as described below.

Figure 1 shows the $x-t$ diagram of the CD-ST in the planar shock wave–grid turbulence interaction experiment. In the coordinate system, the x -axis is directed from the left diaphragm to the right, and the Δx -axis is directed from the grid location to the left (which is the same direction in which the grid turbulence advances). The y -axis is defined with its origin at the bottom inner wall and is directed to an upper wall. The z -axis origin is located at the front inner wall and is directed to the opposite wall. A square grid containing $5 \text{ mm} \times 5 \text{ mm}$ square pillars with a mesh size of 25 mm is located at $x = 5.00 \text{ m}$ in the setup shown in Fig. 1. To weaken the shock wave such that it is weaker than $M_s = 1.03$, sheets of punched metal are installed at $x = 1.0 \text{ m}$ as necessary. In the experiment, the following series of events occurs in the CD-ST. First, the right-side incident shock wave R-iSW proceeds in the left direction after breaking the diaphragm of the right-side driver section. When R-iSW reaches the square grid, a grid-transmitted shock wave R-gSW propagates toward the left, and a weak grid-reflected shock wave R-rSW proceeds in the right direction. The uniform flow behind R-iSW experiences compression because of R-rSW. Then, the flow becomes the grid turbulence when it passes through the square grid from the right to the left. Conversely, the left-side incident shock wave L-iSW propagates toward the right following the rupture of the left-side diaphragm after a delay time τ . At a certain point in the driven section, a head-on collision occurs between R-gSW and L-iSW, and these shock waves become the transmitted shock waves R-tSW and L-tSW, respectively. The shock wave L-tSW meets the grid turbulence proceeding to the left, and interaction between

the planar shock wave and grid turbulence occurs. The interaction length L_i is defined as the distance from the head of the grid turbulence to the shock wave arriving at the center of the visualization window. By setting the delay time τ between the incident shocks generated by the two drivers, L_i can be well controlled.

In the experiment using the CD-ST, three control parameters decide the condition of interaction. The initial pressure ratio between the left driver section and the driven section, p_{4L}/p_1 , primarily determines the shock Mach number of L-tSW $M_{s, L-tSW}$, during the interaction with the grid turbulence. The right-side initial pressure ratio p_{4R}/p_1 decides the shock Mach number of R-iSW $M_{s, R-iSW}$. Because R-iSW has a one-to-one relationship with the turbulence mean velocity, p_{4R}/p_1 determines the turbulence Mach number M_t of the grid turbulence. The delay time between the left and right incident shock generations, τ , determines the collision point of the incident shock wave in the same set of $(M_{s, L-tSW}, M_t)$ and then controls the interaction length L_i . In this experiment, we evaluated the effects of the three parameters $M_{s, L-tSW}$, M_t , and L_i by properly setting the values of p_{4L}/p_1 , p_{4R}/p_1 , and τ .

The shadowgraph and schlieren methods were used to visualize the shock wave propagation through the grid turbulence. The visualization system consisted of a high-speed camera (Phantom v1211, Vision Research Inc.; 256×256 pixels, 100 kfps) and synchronized pulse diode laser (CAVILUX Smart, Cavitar Ltd.; wavelength = 640 nm, pulse duration = 10 ns). This system visualized the shock wave before and during the interaction with the grid turbulence at a pair of BK7 windows (effective diameter $\varphi = 110$ mm) installed on the sidewall at $\Delta x = 0.45$ m. The optical path from the test section to the high-speed camera was approximately 20 m to facilitate the capture of weak density changes with high sensitivity.

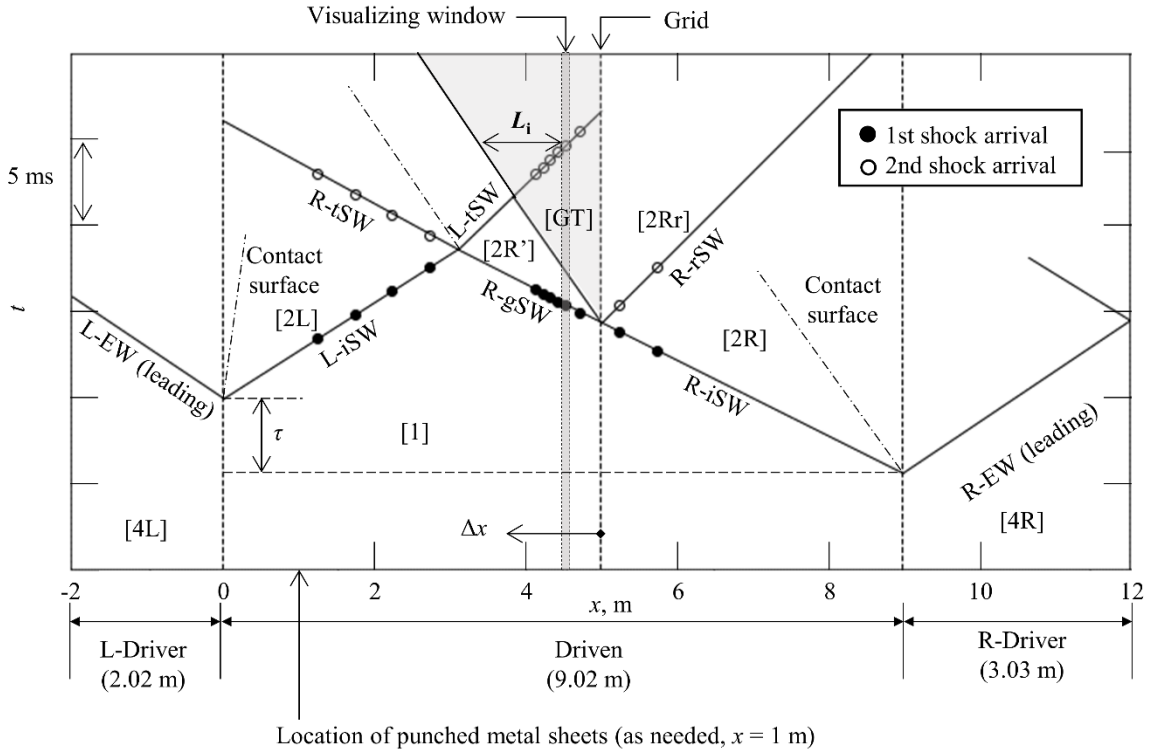


Fig. 1 Example of x - t diagram of shock-turbulence interaction for $M_{s,L-iSW} = 1.05$, $\tilde{M}_t = 0.014$, and $L_i = 1185$ mm.

In a diaphragm-type shock tube, the generation of a weak planar shock wave is difficult because the diaphragm's opening time becomes longer under small pressure differences between the driver and driven sections [Ref32]. When the left-side initial pressure difference $p_{4L} - p_1$ was smaller than 20 kPa, an 18 μm thick cellophane sheet was used for the diaphragm. The minimum pressure difference of the diaphragm required to form a planar shock wave in the test section was approximately 8 kPa. In this case, because the shock Mach number was approximately $M_{s,L-iSW} = 1.04$, the planar shock wave needed to be weakened to generate the shock with a Mach number of 1.01. To generate a weakened shock, we installed sheets of punched metal with small holes in the shock tube at $x = 1.0$ m using a flange. The shock Mach number became small when the shock wave

was transmitted through the punched metal sheets [\[Ref33\]](#). When the shock wave passed through three sheets of punched metal with a thickness d of 1 mm, hole diameter ϕ of 2 mm, and blocking ratio σ of 64%, the M_s value of the wave decreased from 1.05 to 1.03. To generate a weakened shock wave with a Mach number of 1.01, we used 16 sheets of punched metal with d of 0.8 mm, ϕ of 1 mm, and σ of 82.5%. Figure 2 shows the pressure history of the shock wave at $x = 1.25$ m after it passed through the 16 sheets of punched metal. The pressure rise time for the shock wave L-iSW after it passed through the punched metal sheets was shorter than 20 μ s. This time was close to the time resolution obtained when a weak shock wave passed over a flush-mounted pressure sensor with a thickness of 5.5 mm. We also confirmed the planarity of the weakened shock wave in the optically visualized image. The pressure behind the shock wave was nearly constant. Therefore, a planar shock wave with a Mach number of approximately 1.01 was well generated in the CD-ST.

In our previous study [\[Ref31\]](#), a hot-wire anemometer probe was damaged by debris from the finely ruptured cellophane diaphragm that impinged against it. Because of the damage, the turbulent flow characteristics were not obtained under the strong turbulence condition of the turbulent Mach number of 0.024. In this study, a 100 μ m thick polyester diaphragm was used when the pressure difference between the driver and driven sections exceeded 100 kPa to suppress the debris generation. The polyester diaphragm did not degrade the diaphragm opening performance, and the shock wave formation distance was within the allowable value. Consequently, a hot-wire anemometer probe could be used to measure the grid turbulence with a flow velocity of approximately 160 m/s without any damage to the probe.

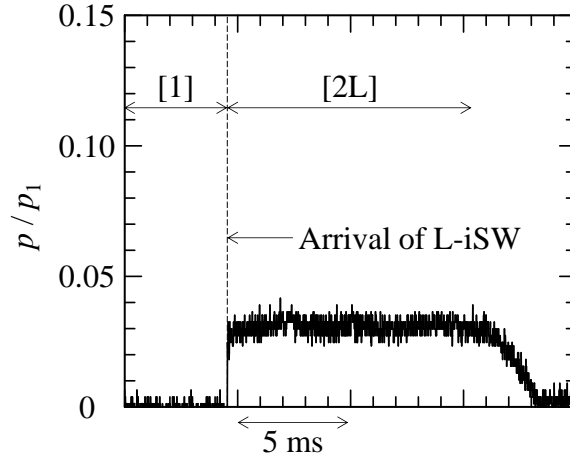


Fig. 2 Example of raw pressure history of L-iSW at $x = 1.25$ m after it passed through 16 sheets of punched metal. The shock Mach number was 1.008.

3. Experimental conditions

This section describes the experimental conditions and the characteristics of the grid turbulence. Table 1 lists the initial pressure conditions and measured shock Mach number. The propagation velocities of L-iSW, R-iSW, and R-gSW were measured by the time-of-flight principle. The shock Mach number M_s was calculated by dividing the shock wave velocity by the speed of sound in the gas in the driven section. We assumed that the gas was calorically perfect: the specific heat ratio was constant ($\gamma = 1.4$). Because L-tSW propagated in a uniform flow behind R-gSW, the shock Mach number was calculated by the pressure jump obtained by the pressure sensor. Here, the static pressure in the states [2R'] and [GT] was constant because the boundary between them was the contact surface.

Table 1 Measured shock wave and grid turbulence characteristics and initial operation conditions

$M_{s, L-iSW}$	\overline{M}_t	p_{4L} (kPa)	p_1 (kPa)	p_{4R} (kPa)	Sheets of punched metal	\tilde{L} (mm)	\overline{Re}_M	\overline{Re}_λ	$M_{s, L-iSW}$	$M_{s, R-iSW}$	$M_{s, R-gSW}$
1.012 ± 0.001	0.005 ± 0.001	61.9	48.2	75.2	$d = 0.8$ mm, $\varphi =$ 1 mm, $\sigma =$ 0.825, 16 sheets	7.9	4.1×10^4	126	1.013 ± 0.001	1.094 ± 0.001	1.089 ± 0.001
1.011 ± 0.001	0.009 ± 0.001	51.3	39.6	93.3		10.3	7.7×10^4	357	1.013 ± 0.000	1.189 ± 0.001	1.179 ± 0.001
1.009 ± 0.003	0.014 ± 0.001	42.0	32.0	138.2		6.0	9.6×10^4	1034	1.014 ± 0.001	1.340 ± 0.006	1.319 ± 0.006
1.029 ± 0.001	0.005 ± 0.001	60.3	48.2	75.2	$d = 1$ mm, $\varphi = 2$ mm, $\sigma = 0.64$, 3 sheets	7.9	4.1×10^4	126	1.031 ± 0.001	1.094 ± 0.000	1.090 ± 0.000
1.026 ± 0.001	0.009 ± 0.001	49.5	39.6	93.3		10.3	7.7×10^4	357	1.029 ± 0.001	1.188 ± 0.001	1.179 ± 0.001
1.021 ± 0.002	0.014 ± 0.001	40.0	32.0	138.2		6.0	9.6×10^4	1034	1.026 ± 0.001	1.341 ± 0.003	1.318 ± 0.005
1.047 ± 0.001	0.005 ± 0.001	61.9	48.2	75.2	w/o	7.9	4.1×10^4	126	1.049 ± 0.001	1.092 ± 0.000	1.088 ± 0.000
1.047 ± 0.003	0.009 ± 0.001	51.3	39.6	93.3		10.3	7.7×10^4	357	1.050 ± 0.001	1.188 ± 0.001	1.179 ± 0.001
1.047 ± 0.002	0.014 ± 0.001	42.0	32.0	138.2		6.0	9.6×10^4	1034	1.053 ± 0.002	1.341 ± 0.002	1.317 ± 0.002
1.105 ± 0.001	0.005 ± 0.001	80.2	48.2	75.2		7.9	4.1×10^4	126	1.110 ± 0.000	1.094 ± 0.000	1.090 ± 0.001
1.100 ± 0.001	0.009 ± 0.001	65.9	39.6	93.3		10.3	7.7×10^4	357	1.111 ± 0.000	1.190 ± 0.000	1.180 ± 0.001
1.150 ± 0.001	0.005 ± 0.001	97.8	48.2	75.2		7.9	4.1×10^4	126	1.157 ± 0.000	1.095 ± 0.000	1.091 ± 0.001
1.150 ± 0.002	0.009 ± 0.001	82.7	39.6	93.3		10.3	7.7×10^4	357	1.163 ± 0.001	1.189 ± 0.001	1.180 ± 0.001

The state [GT] underwent compression because of the grid-reflected shock R-rSW. Thus, the temperature in the state [GT] was higher than that in the upstream uniform flow [2R']. To quantify the grid turbulence characteristics, we measured the total temperature and velocity using cold- and hot-wire anemometers. The total temperature was measured by varying the x - and y -direction values and fixing the z -direction value at 60 mm. The measurement range in the y -direction was $5 < y < 60$ mm, and flow symmetry was assumed for $y > 60$ mm. Figure 3 shows the normalized mean total temperature in the state [GT] for the initial temperature in the driven section T_1 in the same Δx plane. The error bars represent the standard deviations. The measurement point in the y -direction was changed while maintaining the same distance from the grid Δx . The measurement plane was $\Delta x = 0.45$ and 0.75 m for $M_{s, R-gSW} = 1.09$ and $\Delta x = 0.45$ and 0.95 m for $M_{s, R-gSW} = 1.18$ and 1.32 . A nearly uniform temperature field was formed at $20 > y > 60$ mm for all conditions. Total temperature uniformity was maintained in the y -direction for the measured range in the Δx -direction. The total temperature in the region represented by $0 < y < 20$ mm was lower than that in the central area. On the yz -plane with $\Delta x = 0.45$ m, the total temperatures measured at $y = 60$ and 10 mm were different: approximately 3, 4.5, and 8 K under the conditions of $M_{s, R-gSW} = 1.09, 1.18,$ and 1.32 , respectively. This low-temperature field was generated because of the wall effects. The grid size ($m = 25$ mm) was considered to have a dominant effect on the creation of the low-temperature region because the low-temperature region was similar ($0 < y < 20$ mm) for all grid turbulences. The measurement results found that the core region of the grid turbulence was approximately $80 \text{ mm} \times 80 \text{ mm}$ in the center of the CD-ST under the symmetrical condition assumption. Thus, in this experiment, only the phenomena around the center of the CD-ST were evaluated.

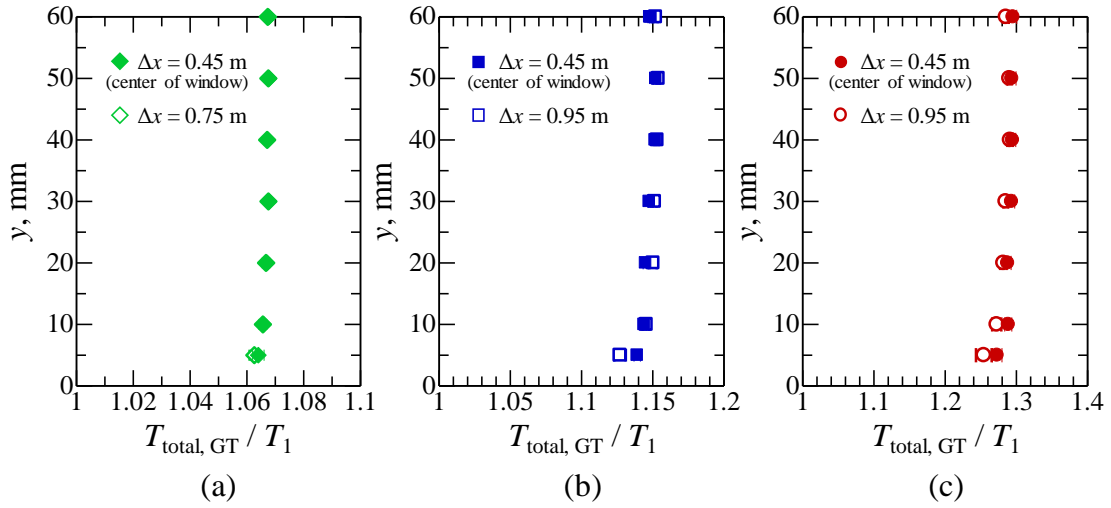


Fig. 3 Distribution of the normalized total temperature of the grid turbulence in the y -direction: **a** $M_{s, R-gSW} = 1.09$, **b** $M_{s, R-gSW} = 1.18$, and **c** $M_{s, R-gSW} = 1.32$

An I-type constant-temperature hot-wire anemometer was calibrated based on the obtained total temperature information, and the velocity was measured. Further information of the calibration method of the hot-wire anemometer is described in our previous study [\[Ref31\]](#). Figure 4 shows the turbulence Mach number of the grid turbulence as a function of the distance from the grid Δx . The measurement point was the shock tube center: $y = z = 60$ mm. We confirmed isotropic characteristics in velocity fluctuations between x - y (u - v) and x - z planes (u - w components). The isotropic nature of the grid turbulence generated in the shock tube has already been confirmed in previous experimental research. According to the experiment by Agui et al. [28], the measurement of three velocity components supported that the grid generated turbulence in the shock tube was isotropic. Our condition of the grid turbulence characteristics, such as the mesh Reynolds number, were close to their experiment. Then the turbulent Mach number was calculated using the measured x -component of the velocity fluctuation u'_x , assuming that the grid turbulence was isotropic. Thus, the relationship $M_t = u' / a_{GT} = \sqrt{3} u'_x / a_{GT}$ was used, where a_{GT} is the speed of sound in the grid turbulence. A typical power law decay of M_t in

space was observed. The decay constant n of the grid turbulence, expressed as $(u' / U)^2 = (\Delta x / m)^{-n}$, was 0.9, 1.2, and 0.3 for $M_{s,R-gSW} = 1.09, 1.18$ and 1.32, respectively, where U is the mean velocity of the grid turbulence. The decay tendency and value of n were consistent with the grid turbulence measurement results generated in a wind tunnel and shock tube in previous studies $\text{\cite{Ref34,Ref35,Ref36}}$. Some parameters of the grid turbulence change with increasing distance from the grid. To distinguish these values changing depending on the distance from the grid, we express the representative value using a tilde. For example, the representative of the turbulent Mach number was presented as \widetilde{M}_t . Here, the representative values were adopted for the value at $\Delta x = 0.45$ m, and $\Delta x = 0.45$ m was a location in the center of the window where the shock wave was visualized by the optical method. The representative value of the turbulence Mach number was $\widetilde{M}_t = 0.005, 0.009$, and 0.014 for $M_{s,R-gSW} = 1.09, 1.18$, and 1.32, respectively. Table 1 also lists the representative values of the integral scale \widetilde{L} , mesh Reynolds number $Re_M = U m / \nu$, and turbulent Reynolds number based on the Taylor microscale $Re_{\lambda} = \langle u' \rangle \lambda / \nu$, where ν is the kinematic viscosity; $\langle u' \rangle$ is the root mean square of the velocity fluctuations, and λ is the Taylor microscale.

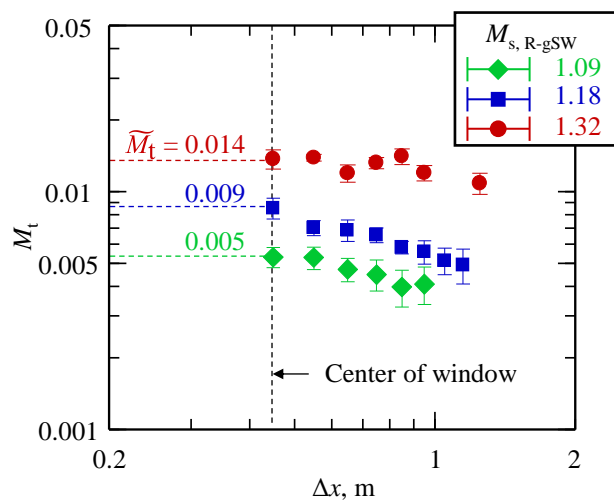


Fig. 4 Turbulent Mach number as function of distance from the grid

4. Results and discussion

4.1 Visualization of interaction of planar shock wave with grid turbulence

In this section, we discuss the qualitative study of the projected shock wave images. The shadowgraph and schlieren methods were used to visualize the shock wave propagation through the grid turbulence as described in Section 2. The proceeding direction of the planar shock wave was from the left to the right, and the grid turbulence direction was from the right to the left, as shown in Fig. 1. To eliminate stationary noise, such as scratches on the window, a reference image was subtracted from the obtained images; the images included in this study are the differential images obtained after subtraction. Here, the reference image was obtained at a quiescent gas state before operation of the CD-ST.

Figure 5 shows the projected images of the planar shock wave with $M_{s, L-tSW} \approx 1.01$ interacting with the grid turbulence. The horizontal axis represents the dimensionless interaction length normalized by the representative value of the integral length scale of the grid turbulence, L_i / \tilde{L} , whereas the vertical axis represents the turbulence Mach number. The images enclosed in solid- and dashed-line frames were visualized by the shadowgraph and schlieren methods, respectively. An area of approximately 80 mm in height in the center of the shock tube was extracted as the evaluation region. A negative value of L_i / \tilde{L} indicated that the shock wave had not begun its interaction with the grid turbulence. Under all conditions, the shock wave was nearly planar with $L_i / \tilde{L} < 0$. In the interaction with the weakest turbulence ($\tilde{M}_t = 0.005$), the projected thickness of the shock wave increased

with an increase in L_i / \tilde{L} . At $L_i / \tilde{L} = 41.6$, some lines showing density changes were observed because the multidimensionally deformed shock wave was observed from the side view. For the interaction with the grid turbulence at $\tilde{M}_t = 0.009$, the shock waves were not easily detected by the shadowgraph method when L_i / \tilde{L} was above 33.7. In the schlieren method, the deformation of the shock wave was observed even for $L_i / \tilde{L} = 33.7$. The brightness representing the density gradient by the shock wave showed a dispersed profile in the x - and y -directions. For the interaction with the strongest turbulence ($\tilde{M}_t = 0.014$), the shock wave was deformed by the turbulence at $L_i / \tilde{L} = 26.4$. When L_i / \tilde{L} was above 42.5, the density changes in the projected image of the shock wave became considerably weak. In the shadowgraph and schlieren methods, the visualized shock wave exhibited a dispersed profile. For $L_i / \tilde{L} > 100$, the density changed because the shock wave resulted in the loss of the sharp lines, which was observed in the initial stage of the interaction. The projected shock wave region weakened and expanded in the traveling direction, and we could not easily detect the edge of the shock wave. Online Resource 1 and 2 show the schlieren movies of the interaction. The shock Mach number of the interacting shock wave was $M_{s, L-tSW} = 1.009 \pm 0.003$, and the turbulence Mach number of the grid turbulence was $\tilde{M}_t = 0.014 \pm 0.001$. In Online Resource 1, the shock wave collided with the grid turbulence in the center of the visualized window. At the beginning of the interaction, the shock wave maintained its planar profile. Online Resource 2 shows the visualization of the shock wave when L_i / \tilde{L} was above 250. The sharp line representing the shock wave vanished. The widely dispersed density change region progressed in the turbulent field from the right to the left. In the comparison between Online Resource 1 and 2, the shock wave deformation gradually proceeded depending on L_i / \tilde{L} with the grid turbulence. Therefore, L_i / \tilde{L} affected the shock wave

behavior in the turbulent field even when \widetilde{M}_t was at the same level.

Figure 6 shows the images of the shock waves with $M_{s, L-tSW} = 1.02\text{--}1.03$ interacting with the grid turbulence. For the interaction with the turbulence at $\widetilde{M}_t = 0.005$, the shock wave was planar even while it proceeded through the turbulence. In this condition, the projected thickness of the shock wave slightly increased because of the turbulence. For the grid turbulence at $\widetilde{M}_t = 0.009$, the shock waves were detected during the entire interaction, and the projected thickness was greater than that of $\widetilde{M}_t = 0.005$ under approximately the same L_i / \widetilde{L} . For the interaction with the strongest turbulence ($\widetilde{M}_t = 0.014$), the shock wave was planar until $L_i / \widetilde{L} > 46.2$. When L_i / \widetilde{L} was above 53.3, the shock wave dispersed in the x -direction. Numerous lines remained relatively sharp in the visualized region. For the shadowgraph and schlieren methods, the shock wave lost the single line profile and locally disappeared on the projected images. However, unlike the weak shock wave of $M_{s, L-tSW} \approx 1.01$, the sharp lines did not vanish entirely.

Figures 7–9 show the projected side-view images of the shock–turbulence interaction when the Mach numbers of the planar shock wave were 1.05, 1.10, and 1.15. Unlike the interaction involving the weaker shock wave with $M_{s, L-tSW} < 1.03$, the shock waves did not show a dispersed profile. The line representing the change in the density of the shock wave remained sharp in the entire y -direction.

As conclusion of this section, for the interaction involving the weak shock waves with $M_{s, L-tSW} < 1.03$, the projected thickness of the shock waves increased with an increase in L_i / \widetilde{L} . Under the same intensity of the shock wave, the projected thickness of the shock wave propagating in the grid turbulence became large with an increase in the turbulent Mach number. When the intensity of the grid turbulence was the same, an increase in

$M_{s, L-tsw}$ prevented an increase in the projected thickness of the shock wave against increases in \bar{M}_t and L_i / \bar{L} .

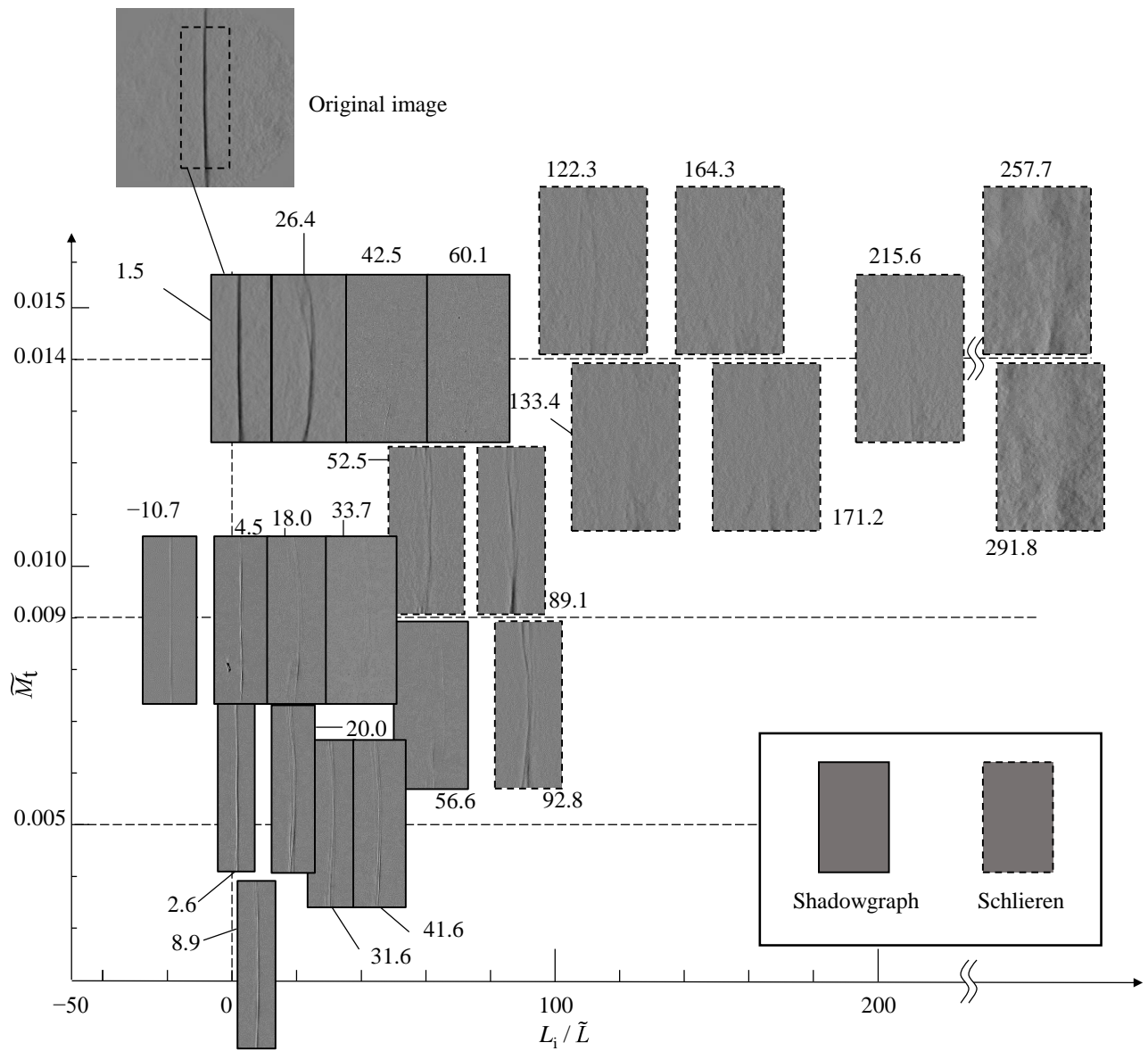


Fig. 5 Projected images of the shock wave propagating through the grid turbulence for $(M_{s, L-tsw}, \bar{M}_t) = (1.012 \pm 0.001, 0.005 \pm 0.001)$, $(1.011 \pm 0.001, 0.009 \pm 0.001)$, and $(1.009 \pm 0.003, 0.014 \pm 0.001)$. The central area from $y = 20$ to 100 mm was extracted from the differential images.

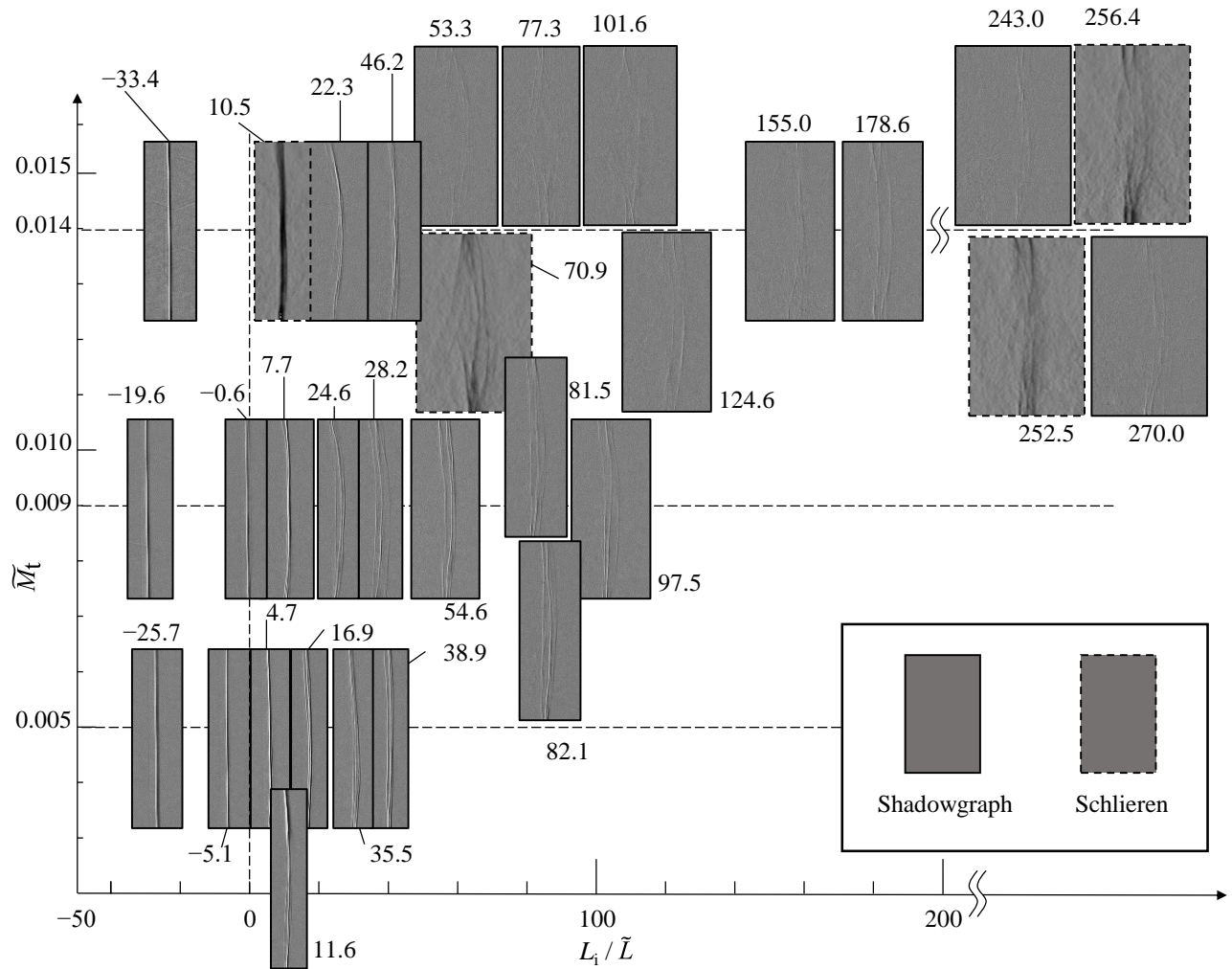


Fig. 6 Projected images of the shock wave propagating through the grid turbulence for $(M_{s, L-tSW}, \bar{M}_t) = (1.029 \pm 0.001, 0.005 \pm 0.001)$, $(1.026 \pm 0.001, 0.009 \pm 0.001)$, and $(1.021 \pm 0.002, 0.014 \pm 0.001)$.

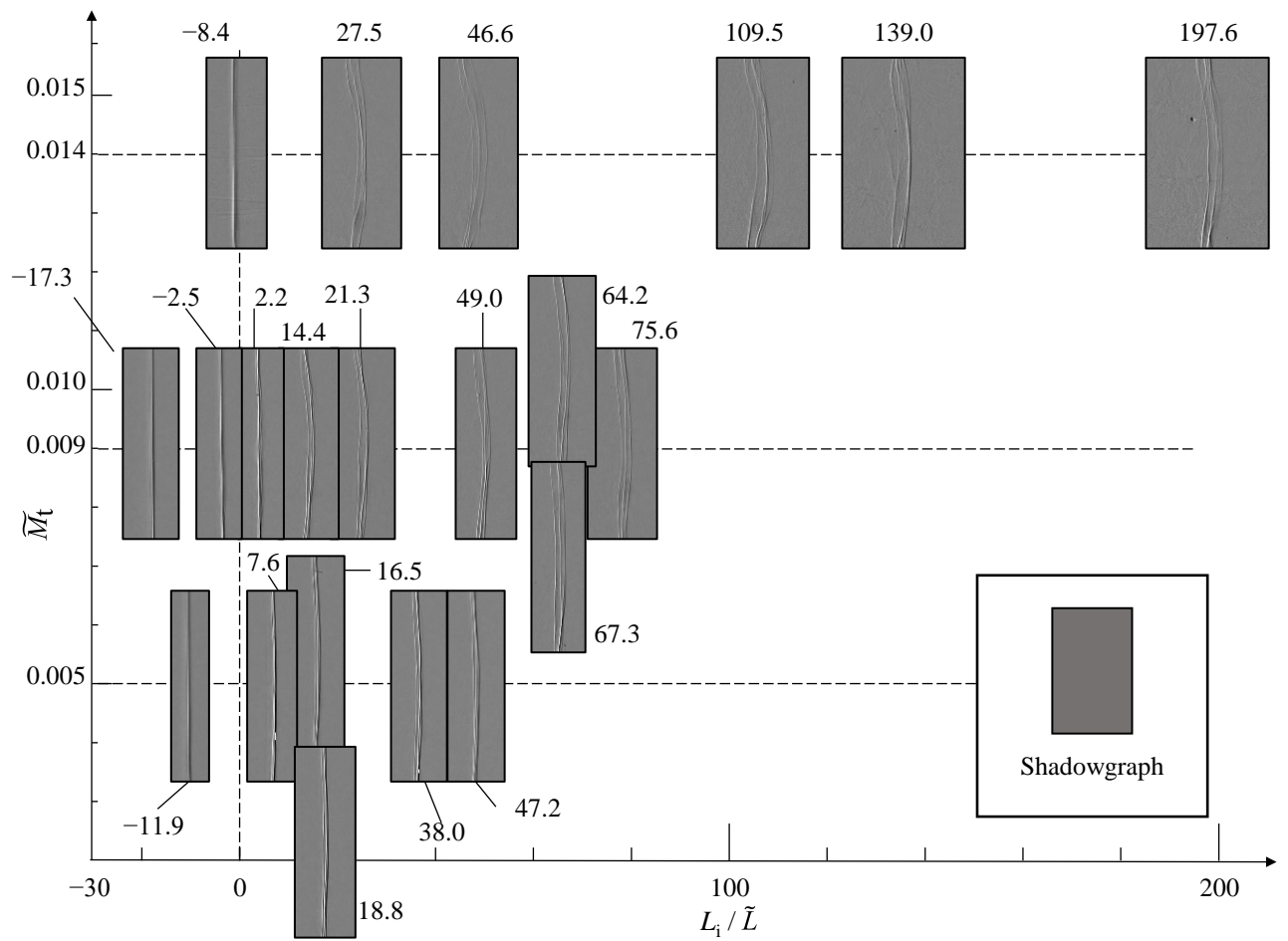


Fig. 7 Projected images of the shock wave propagating through the grid turbulence for $(M_{s, L-tSW}, \tilde{M}_t) = (1.047 \pm 0.001, 0.005 \pm 0.001)$, $(1.047 \pm 0.003, 0.009 \pm 0.001)$, and $(1.047 \pm 0.002, 0.014 \pm 0.001)$.

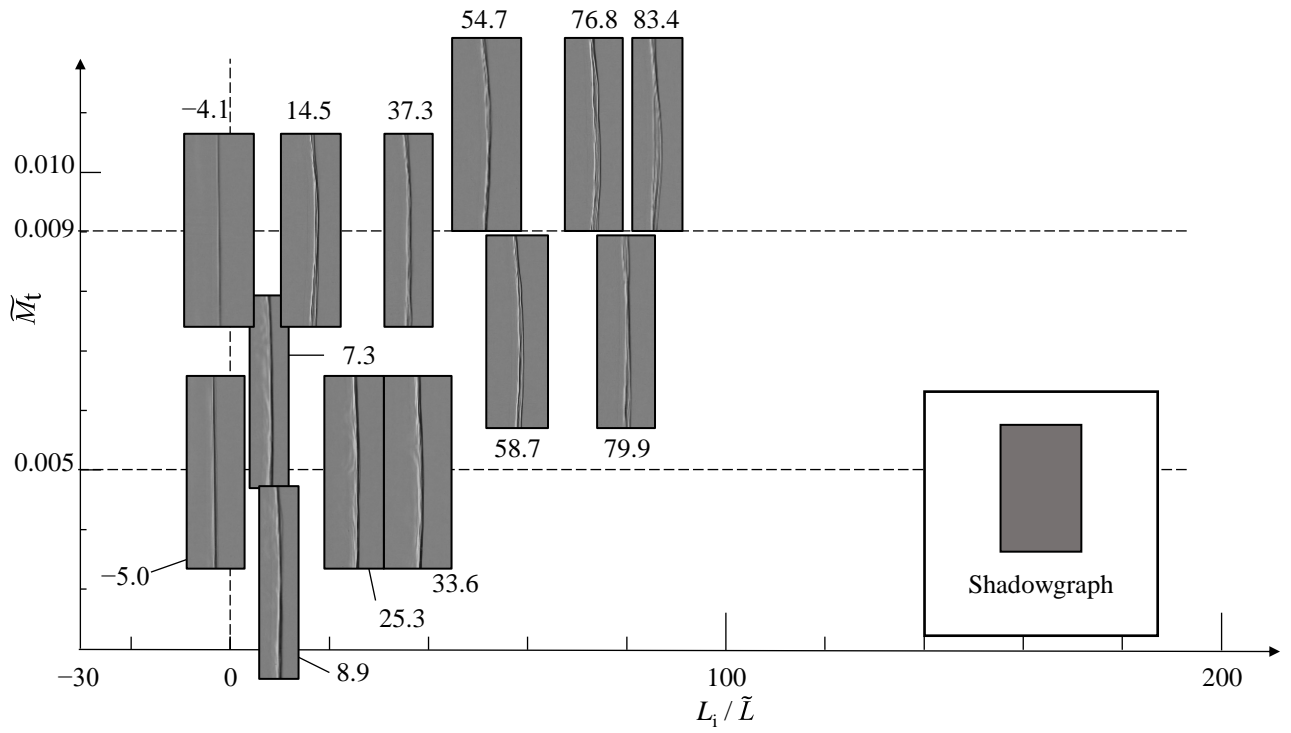


Fig. 8 Projected images of the shock wave propagating through the grid turbulence for $(M_{s,L-tSW}, \tilde{M}_t) = (1.105 \pm 0.001, 0.005 \pm 0.001)$ and $(1.100 \pm 0.001, 0.009 \pm 0.001)$.

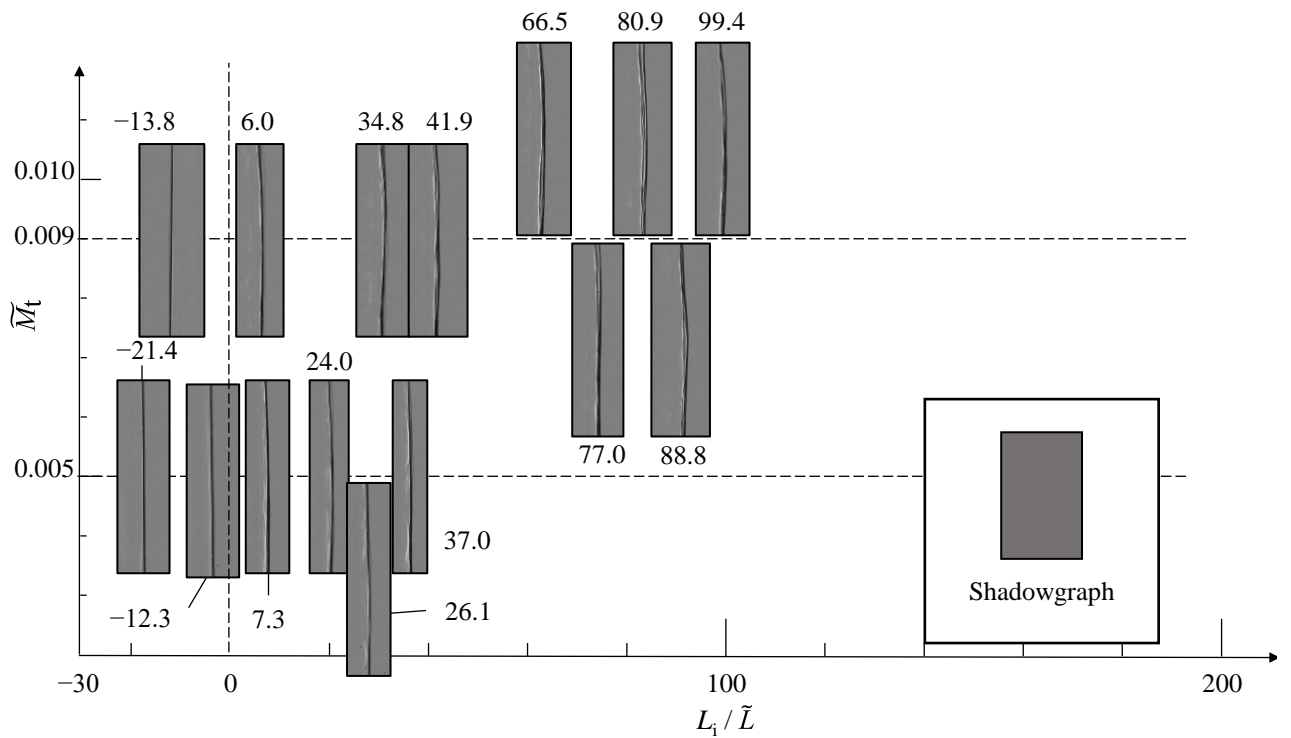


Fig. 9 Projected images of the shock wave propagating through the grid turbulence for $(M_{s,L-tSW}, \tilde{M}_t) = (1.150 \pm 0.001, 0.005 \pm 0.001)$ and $(1.150 \pm 0.002, 0.009 \pm 0.001)$.

4.2 Edge profile and thickness of the projected shock wave

We analyzed the projected images to investigate the planar shock modulations owing to the grid turbulence. We evaluated the edge profile and thickness in the projected images captured from the side view. In the typical schlieren and shadowgraph method, information in the same direction as the light path (the z -direction in this study) is integrated and shown on an image. Therefore, if the shock wave was not detected on the projected images, the shock wave was considered to locally lose a sharp density change in the x -direction for the entire light path direction. In this shock wave edge analysis, the evaluation range was N_y pixels in the y -direction around the center of the shock tube and all the pixels in the x -direction. The value of N_y was 80 in this analysis (approximately 32 mm in the y -direction). The edges in the projected image were extracted by the Canny method. Figure 10 shows an example of the left and right edges of the shock wave detected in the analyzed area. In the location where the edge was not found, the shock wave could lose a discontinuous property change profile in the x -direction for the entire z -direction. In a certain point y_i in the y -direction, where i represents a sequential number, the existence of the shock wave was evaluated in the x -direction. This operation continued from $i = 0$ to N_y . Then, the number of pixels in which the shock wave was not found in the y -direction, $N_{y, w/o\ shock}$, was counted. The undetectable ratio of the shock wave α was defined as the ratio of the y -direction pixels where the shock wave front did not exist throughout the x -direction and was calculated as follows:

$$\alpha = \frac{N_{y, w/o\ shock}}{N_y} \quad (1)$$

Figure 11 shows the dependence of α on L_i / \tilde{L} . The same process was applied to the shadowgraph and schlieren

images. The undetectable ratio of the projected shock wave obtained from the shadowgraph (closed symbol) and schlieren (open symbol) images indicated nearly the same tendency except under some conditions. Figure 11(a) shows the undetectable ratio variations of the interacting shock wave with $M_{s, L-tSW} \approx 1.01$. For the interaction with the weakest turbulence ($\widetilde{M}_t = 0.005$), the undetectable ratio was 0 during the entire observed interaction. In the interaction with $\widetilde{M}_t = 0.009$, the projected shock wave locally lost its edge when L_i / \widetilde{L} exceeded 20. Then, the value of α was in the range of 0.1–0.4 at $L_i / \widetilde{L} \approx 40$. In the schlieren image obtained at $L_i / \widetilde{L} \approx 90$, the undetectable ratio returned to zero. However, only under this condition, the shadowgraph and schlieren images could be considered to yield different values of α owing to the difference in the detection sensitivity. For the interaction with the strongest turbulence ($\widetilde{M}_t = 0.014$), the undetectable ratio sharply increased above $L_i / \widetilde{L} = 30$ and nearly reached unity when L_i / \widetilde{L} was above 100. The visualized image in Fig. 5, whose undetectable ratio was approximately 1, showed that the shock wave lost the sharp profile, demonstrating continuous property changes in the x -direction.

The shock wave with $M_{s, L-tSW} = 1.02$ – 1.03 (Fig. 11(b)) showed a perfectly detectable profile in the interaction with the grid turbulence at $\widetilde{M}_t = 0.005$ and 0.009 . For the interaction with the strongest turbulence ($\widetilde{M}_t = 0.014$), the undetectable ratio started to increase at approximately $L_i / \widetilde{L} = 50$ and obtained a value in a range of 0.1–0.5 at $L_i / \widetilde{L} > 250$. The relatively strong shock waves with $M_{s, L-tSW} = 1.05$, 1.1 , and 1.15 showed detectable profiles on the projected images under all the conditions of the grid turbulence: the undetectable ratio was zero (Fig. 11(c)–(e)).

In the shock wave edge analysis on the projected images, the shock–turbulence interactions for $(M_{s, L-tSW}, \widetilde{M}_t)$

$\approx (1.01, 0.009)$, $(1.01, 0.014)$, and $(1.02, 0.014)$ indicated an undetectable profile of the shock wave on the projected image when L_i / \tilde{L} reached approximately 20–50. These three conditions were the cases in which the shock wave was weak, and the turbulence was relatively intense. In addition, these conditions satisfied the appearance of the broken shock criterion: $M_t \geq 0.6 (M - 1)$, in which the shock wave front could become subsonic, as proposed by Donzis [16] and Larsson et al. [99]. Because the projected images of the shock wave were obtained by the optical system whose sensitivity remained constant throughout the experiments, our experimental results showed the consistency with previous DNS studies, although shadowgraph and schlieren visualization depends on the sensitivity in general. On the other hand, there is a difference between the experimental and numerical studies. Our experimental results emphasize the dependence of the shock wave profile on the normalized interaction length L_i / \tilde{L} . This aspect has not been investigated in detail in numerical studies. To clarify the relationship between the experimental results in this paper and the DNS study, a systematic analysis and comparison should be performed in future research.

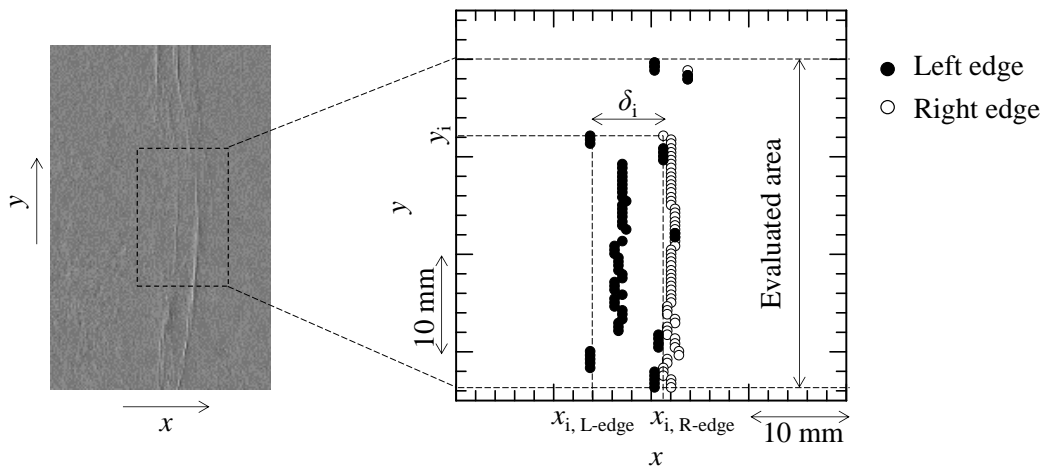


Fig. 10 Example of the detected shock edge from the shadowgraph image for $(M_{s, L-tSW}, \tilde{M}_t, L_i / \tilde{L}) = (1.021 \pm 0.002, 0.014 \pm 0.001, 124.6)$.

Next, the projected thickness of the shock wave region was evaluated. The projected thickness of the shock wave is the important parameter which corresponded to the deformation extent of the shock wave in the x -direction. The projected shock wave region for $y = y_i$ was defined as the distance between the left and right edges and expressed as $\delta_i = x_{i, \text{L-edge}} - x_{i, \text{R-edge}}$. The average value of δ_i in the range $i = 0$ to N_y was defined as the projected shock wave thickness δ . Here, the averaging operation was only carried out for y_i , where the shock thickness was definable. In a shadowgraph method, a second derivative of the density change is expressed as a change in brightness. Because a single planar shock wave had a light area and dark area in the image, the minimum shock wave thickness was two pixels on the obtained image. A pixel in the projected image corresponded to approximately 0.4 mm. Therefore, the resolvable minimum thickness of the shock wave region obtained from the image was approximately 0.8 mm. Under all conditions, δ before interaction with the grid turbulence was approximately 1–2 mm. This thickness was the limit resolution of the shock wave on the images, and this resolution did not correspond to the actual thickness of the shock wave. However, after the shock wave entered the grid turbulence, the projected thickness of the shock wave increased with increasing interaction length. Therefore, the projected thickness δ / \tilde{L} reflects the deformation region of the shock wave in the x -direction by the turbulence interaction, and we evaluated δ / \tilde{L} as the deformation extent of the shock wave.

In Fig. 12, the dimensionless projected thickness normalized by the integral scale of the grid turbulence δ / \tilde{L} is shown as a function of L_i / \tilde{L} . The value of δ / \tilde{L} of the weakest shock wave with $M_{s, \text{L-tSW}} \approx 1.01$ (Fig. 12(a)) increased after the shock wave interacted with the grid turbulence. The value of δ / \tilde{L} was 0.2–0.4 at $L_i / \tilde{L} > 20$. In the interaction with the turbulence at $\tilde{M}_t = 0.009$ and 0.014, the shock wave was deformed

considerably by the grid turbulence. Because the projected image showed a discontinuous profile and did not maintain sharp lines, the projected thickness of the shock wave region was difficult to precisely define. In the interaction of the shock waves with $M_{s,L-tSW} \approx 1.02-1.03$ (Fig. 12(b)), δ / \tilde{L} of the shock region increased rapidly when L_i / \tilde{L} was 0–50. In the interaction with the turbulence at $\tilde{M}_t = 0.005$ and 0.009, the normalized projected thickness became approximately 0.4 and 0.5, respectively, at $L_i / \tilde{L} = 40$. In the interaction with the turbulence at $\tilde{M}_t = 0.014$, the shock wave region expanded greatly. When L_i / \tilde{L} was above 53.5, the shock wave dispersed, and at $L_i / \tilde{L} = 30$, the value of δ / \tilde{L} reached 0.5. Because this value was close to the standard deviations of the average thickness, the expansion and partial disappearance of the shock wave were confirmed. The value of δ / \tilde{L} with $M_{s,L-tSW} \approx 1.05$ (Fig. 12(c)), whose discontinuity ratio was 0 under all interactions, increased moderately compared to the thickness of the weaker shock waves. As the turbulent Mach number increased, the increase in δ / \tilde{L} became slightly steeper. For the shock waves with $M_{s,L-tSW} = 1.1$ and 1.15 (Fig. 12(d) and (e)), the value of δ / \tilde{L} before and during the interaction with the grid turbulence at $\tilde{M}_t = 0.005$ remained the same. In the interaction with the grid turbulence at $\tilde{M}_t = 0.009$, δ / \tilde{L} with $M_{s,L-tSW} = 1.1$ and 1.15 were 0.3 and 0.2, respectively, at $L_i / \tilde{L} > 50$. In this case, which involved a strong shock wave, the shock wave front was slightly deformed with the increase in L_i / \tilde{L} .

Under all conditions, the projected thickness of the shock wave region increased with the increase in L_i / \tilde{L} . The maximum value of δ / \tilde{L} was approximately 1.5, that is the largest deformation of the shock wave in the x -direction was same order to the integral scale of the grid turbulence. The gradient of the projected thickness against the changes in L_i / \tilde{L} was different depending on $M_{s,L-tSW}$ and \tilde{M}_t . When the shock wave exhibited the

undetectable profile, the thickness of the shock wave was difficult to define, and the deviation obtained from the side-view image became large. When the shock wave was continuous even after it interacted with the grid turbulence, the projected thickness of the shock wave had a steeper increase with the increase in the turbulent Mach number. The shock Mach number contributed to the robustness of the shock wave against the turbulence. In addition, in Fig. 12 (b) and (c), the value of δ / \tilde{L} became saturated when the interaction length increased. The saturation of the projected thickness occurred because the self-stability of the shock wave and the disturbance by the velocity fluctuation of turbulence were balanced. In a recent direct numerical simulation by Tanaka et al. [37], the statistical location of the moving shock wave entering the turbulence region was studied. Their results show that the root-mean-square value of the local shock wave location gradually increases after the shock wave enters turbulence. When the shock wave propagates approximately ten times of the integral scale of turbulence, the root-mean-square value of the local shock wave location becomes saturated. In our results, as shown in Fig. 12 (b) and (c), approximately 20–50 times of the integral scale was required for the projected thickness to saturate, and this value was the same order as the DNS result. Therefore, the similarity between the experiment and the DNS was confirmed. In order to physically clarify this phenomenon, we need a detailed investigation.

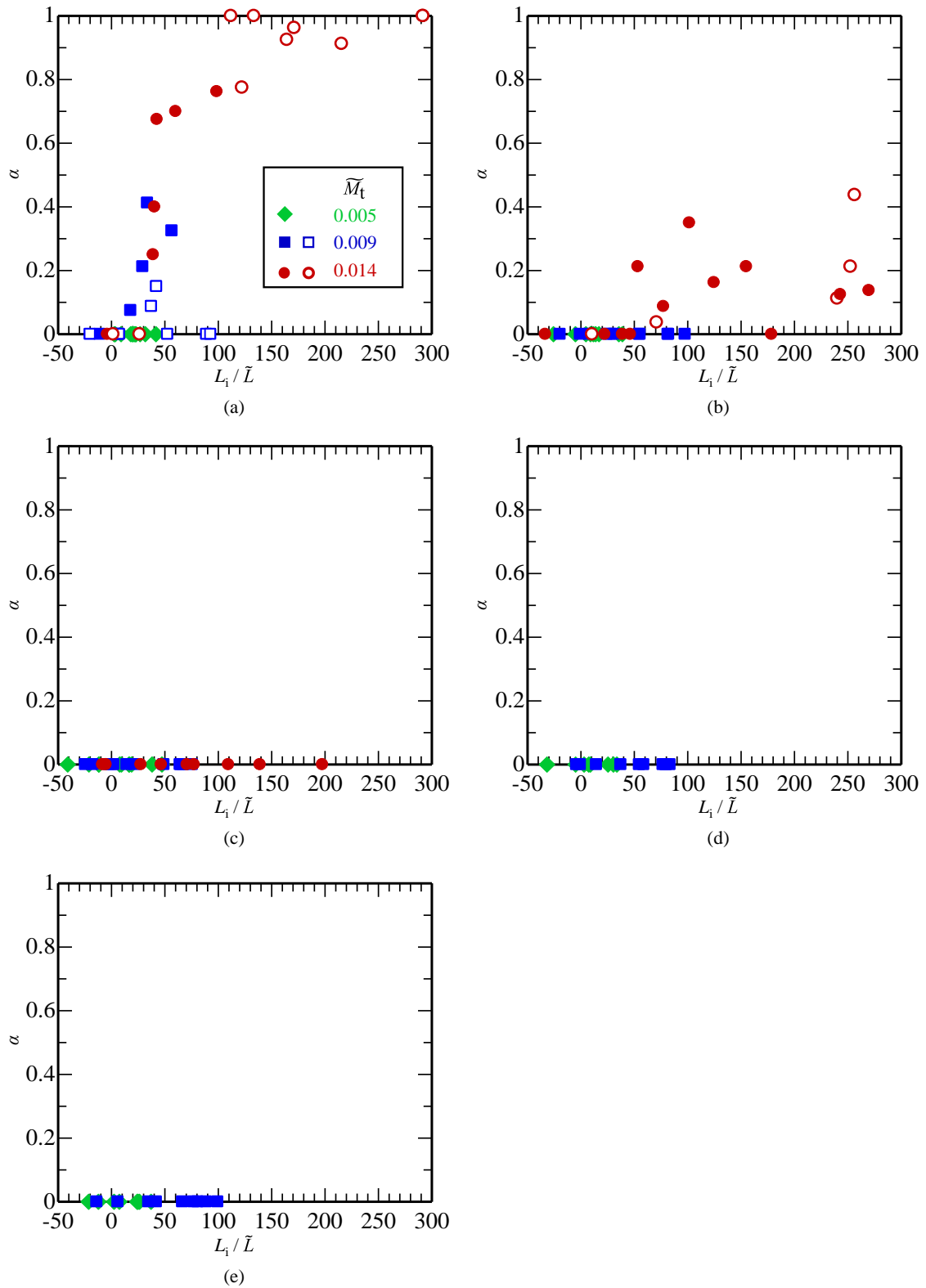


Fig. 11 α vs. L_i / \tilde{L} for **a** $M_{s, L-tsw} \approx 1.01$, **b** $M_{s, L-tsw} \approx 1.02-1.03$, **c** $M_{s, L-tsw} \approx 1.05$, **d** $M_{s, L-tsw} \approx 1.10$, and **e** $M_{s, L-tsw} \approx 1.15$. Closed symbols: results calculated using the shadowgraph image. Open symbols: results calculated using the schlieren image.

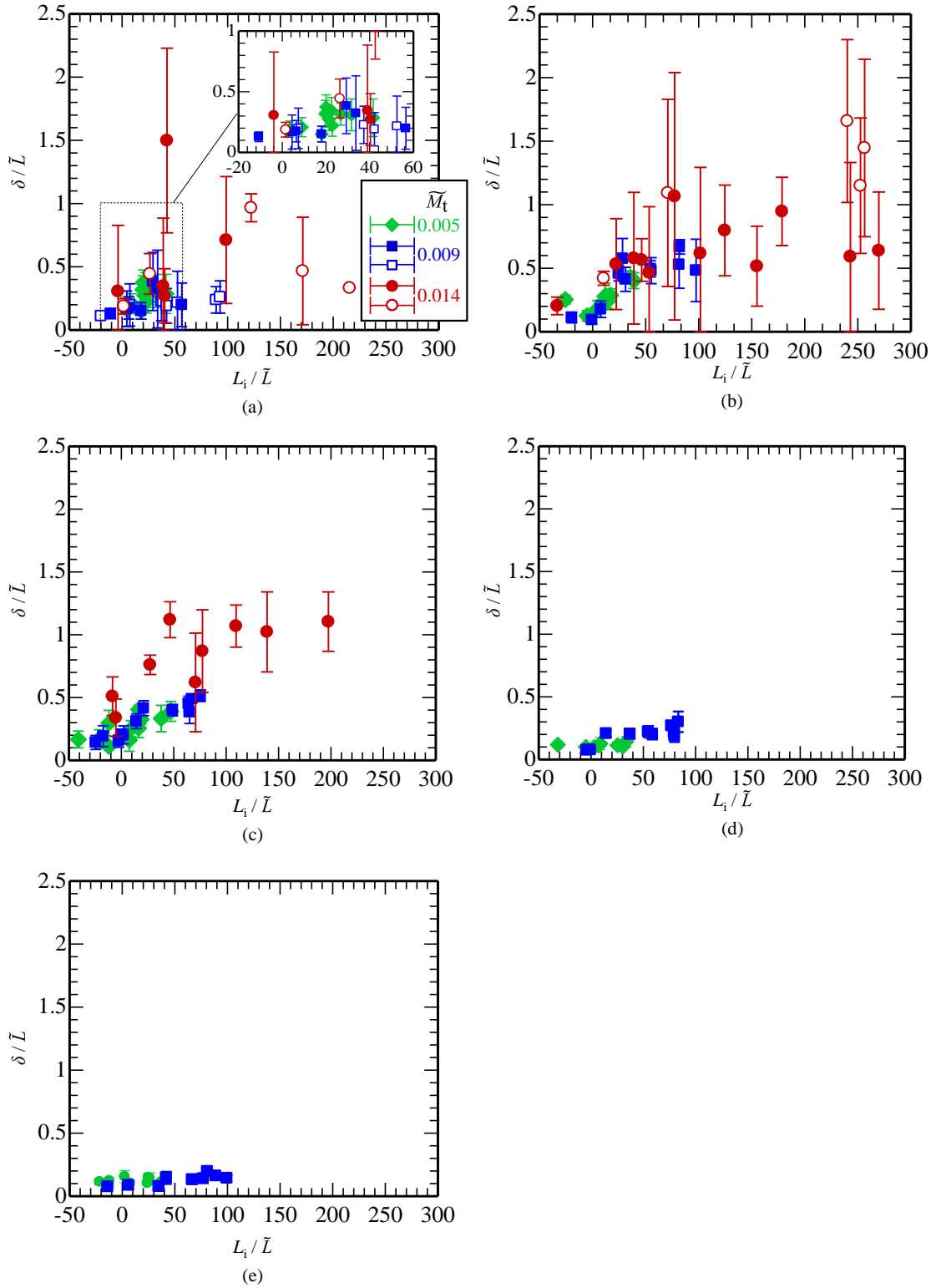


Fig. 12 δ/\tilde{L} vs. L_i/\tilde{L} for **a** $M_{s,L-tSW} \approx 1.01$, **b** $M_{s,L-tSW} \approx 1.02-1.03$, **c** $M_{s,L-tSW} \approx 1.05$, **d** $M_{s,L-tSW} \approx 1.10$, and **e** $M_{s,L-tSW} \approx 1.15$. Closed symbols: results calculated using the shadowgraph image. Open symbols: results calculated using the schlieren image.

5. Conclusion

We investigated the interaction of a planar shock wave with grid turbulence using a counter-driver shock tube. Three parameters, M_s , \widetilde{M}_t , and L_i , were independently controlled. In the grid turbulence formed in the post-shock flow, a temperature variation existed with a height of approximately 20 mm from the wall in a shock tube cross section of 120 mm \times 120 mm; a nearly uniform grid turbulence zone of approximately 80 mm \times 80 mm was formed in the center of the shock tube.

We analyzed the edge profile and thickness of the projected image of the planar shock wave interacting with the grid turbulence. When the turbulence was relatively strong, the planar shock wave exhibited a dispersed profile when it interacted with the turbulence. Extreme shock deformation was observed when the grid turbulence was the strongest ($\widetilde{M}_t = 0.014$), and the shock wave was the weakest ($M_{s, L-tSW} = 1.01$). In the projected shadowgraph and schlieren images where L_i / \widetilde{L} was above 50, the sharp lines of the shock wave vanished entirely. In the interaction with $(M_{s, L-tSW}, \widetilde{M}_t) = (1.02, 0.014)$ and $(1.01, 0.009)$, when L_i / \widetilde{L} was above 50, the shock wave exhibited a undetectable profile on the image. The undetectable ratio on the image was in the range of 0.2–0.5. When the shock wave exhibited a undetectable profile on the image, the relationships between M_s and \widetilde{M}_t satisfied the broken shock criterion $M_t > 0.6 (M - 1)$ proposed in previous studies [cite{Ref9,Ref13,Ref16}](#). Thus, we confirmed the consistency between the experimental results and previous DNS results. On the other hand, in the experiment, L_i / \widetilde{L} greatly affected the profile of the shock wave. Planar shock waves with a Mach number of 1.05 and higher did not show the undetectable profile when they interacted with the grid turbulence at \widetilde{M}_t examined in this study. When the shock wave can be detectable,

the projected thickness of the shock wave increased with an increase in \overline{M}_t , and the saturation of the projected shock wave thickness could be seen in the condition. We consider that the saturation occurred because the self-stability of the shock wave and the disturbance by the velocity fluctuation of turbulence were balanced. Regarding this saturation phenomena, the similarity to the numerical simulation was also confirmed.

In this study, the shock wave profile in a turbulent field was evaluated, and the relationships among the shock Mach number, turbulent Mach number, and interaction length were obtained. In particular, the effects of the interaction length should be further studied because the unsteady shock behavior was greatly influenced by the length effects. The results of this study are important for predicting the behavior of a shock wave unsteadily propagating through a turbulent field, for example, in the modulation of a sonic boom through atmospheric turbulence.

Acknowledgments

The authors gratefully acknowledge the kind donation of the cellophane diaphragm by Futamura Chemical Co., Ltd. We are also grateful for the valuable comments and advice from K. Nagata and T. Watanabe, Nagoya University, and the valuable technical assistance of N. Shiraki, M. Nakakimura, and A. Saito, Technical Division, Nagoya University. This research was supported by the JSPS KAKENHI Grants Nos. 17J10997 and 18H03813.

References

1. Andreopoulos, Y., Agui, J.H., Briassulis, G.: Shock Wave-Turbulence Interactions. *Annu. Rev. fluid. Mech.* **{32}**, 309-345, (2000). <https://doi.org/10.1146/annurev.fluid.32.1.309>
2. Hubbard, H.H., Maglieri, D.J., Huckel, V., Hilton, D.A.: Ground measurements of sonic-boom pressures for the altitude range of 10,000 to 75,000 feet, NASA TR R-198, (1964).
3. Kane, E.J.: Some effects of the atmosphere on sonic boom, NASA SP-147, 49, (1967).
4. Ribner, H.S., Morris, P.J., Chu, W.H.: Laboratory simulation of development of superbooms by atmospheric turbulence. *J. Acoust. Soc. Am.* **{53}**, 926 (1973). <https://doi.org/10.1121/1.1913411>
5. Barre, S., Alem, D., Bonnet, J.P.: Experimental study of a normal shock/homogeneous turbulence interaction. *AIAA J.* **{34}**, 968-974 (1996). <https://doi.org/10.2514/3.13175>
6. Barre, S., Alem, D., Bonnet, J.P.: Reply by the authors to H. S. Ribner. *AIAA J.* **{36}**, 495-495 (1998). <https://doi.org/10.2514/2.398>
7. Lee, S., Lele, S. K., Moin, P.: Direct numerical simulation of isotropic turbulence interacting with a weak shock wave. *J. Fluid Mech.* **{251}**, 533-562 (1993). <https://doi.org/10.1017/S0022112093003519>
8. Larsson, J., Lele, S.K.: Direct numerical simulation of canonical shock/turbulence interaction. *Phys. Fluids* **{21}**, 126101 (2009). <https://doi.org/10.1063/1.3275856>
9. Larsson, J., Bermejo-Moreno, I., Lele, S.K.: Reynolds- and Mach-number effects in canonical shock-turbulence interaction. *J. Fluid Mech.* **{717}**, 293-321 (2013). <https://doi.org/10.1017/jfm.2012.573>
10. Ryu, J., Livescu, D.: Turbulence structure behind the shock in canonical shock–vortical turbulence interaction. *J. Fluid Mech.* **{756}**, R1 (2014). <https://doi.org/10.1017/jfm.2014.477>
11. Livescu, D., Ryu, J.: Vorticity dynamics after the shock–turbulence interaction. *Shock Waves* **{26}**,

241-251 (2016). <https://doi.org/10.1007/s00193-015-0580-5>

12. Tian, Y., Jaber, F.A., Li, Z., Livescu, D.: Numerical study of variable density turbulence interaction with a normal shock wave. *J. Fluid Mech.* **{829}**, 551-588 (2017). <https://doi.org/10.1017/jfm.2017.542>
13. Chen, C.H., and Donzis, D.A.: Shock-turbulence interactions at high turbulence intensities. *J. Fluid Mech.* **{870}**, 813-847 (2019). <https://doi.org/10.1017/jfm.2019.248>
14. Tanaka, K., Watanabe, T., Nagata, K., Sasoh, A., Sakai, Y., Hayase, T.: Amplification and attenuation of shock wave strength caused by homogeneous isotropic turbulence: *Phys. Fluids* **{30}** (3), 035105 (2018). <https://doi.org/10.1063/1.5019867>
15. Donzis, D.A.: Amplification factors in shock-turbulence interactions: Effect of shock thickness, *Phys. Fluids* **{24}**, 011705 (2012). <https://doi.org/10.1063/1.3676449>
16. Donzis, D.A.: Shock structure in shock-turbulence interactions. *Phys. Fluids* **{24}**, 126101 (2012). <https://doi.org/10.1063/1.4772064>
17. Lele, S.K.: Shock-jump relations in a turbulent flow. *Phys. Fluids* **{4}**, 2900 (1992). <https://doi.org/10.1063/1.858343>
18. Lipkens, B., Blackstock, D.T.: Model experiment to study sonic boom propagation through turbulence. *J. Acoust. Soc. Am.* **{103}**, 148 (1998). <https://doi.org/10.1121/1.421114>
19. Kim, J.-H., Sasoh, A., Matsuda, A., Modulations of a weak shock wave through a turbulent slit jet. *Shock Waves* **{20}**, 339-345 (2010). <https://doi.org/10.1007/s00193-010-0265-z>
20. Tamba, T., Furukawa, D., Aoki, Y., Kayumi, M., Iwakawa, A., Sasoh, A., Matsunaga, T., Izumo, M.,

- Sugiyama, Y., Matsumura, T., Nakayama, Y.: Field experiment of blast wave pressure modulation past a turbulent flow. *Sci. Tech. Energetic Materials* **{77}**, 91-97 (2016).
21. Sasoh, A., Harasaki, T., Kitamura, T., Takagi, D., Ito, S., Matsuda, A., Nagata, K., Sakai, Y.: Statistical behavior of post-shock overpressure past grid turbulence. *Shock Waves* **{24}**, 489-500 (2014).
<https://doi.org/10.1007/s00193-014-0507-6>
22. Kitamura, T., Nagata, K., Sakai, Y., Sasoh, A., Ito, Y.: Changes in divergence-free grid turbulence interacting with a weak spherical shock wave. *Phys. Fluids* **{29}**, 065114 (2017).
<https://doi.org/10.1063/1.4984835>
23. Inokuma, K., Watanabe, T., Nagata, K., Sasoh, A., Sakai, Y.: Finite response time of shock wave modulation by turbulence. *Phys. Fluids* **{29}**, 051701 (2017). <https://doi.org/10.1063/1.4982932>
24. Inokuma, K., Watanabe, T., Nagata, K., Sakai, Y.: Statistics of overpressure fluctuations behind a weak shock wave interacting with turbulence. *Phys. Fluids* **{31}**, 085119 (2019).
<https://doi.org/10.1063/1.5110185>
25. Dosanjh, D.S.: Interaction of grids with traveling shock waves. NACA Report No. TN-3680, (1956).
26. Honkan, A., Andreopoulos, J.: Rapid compression of grid-generated turbulence by a moving shock wave. *Phys. Fluids A: Fluid Dyn.* **{4}**, 2562 (1992). <https://doi.org/10.1063/1.858443>
27. Honkan, A., Watkins, C.B., Andreopoulos, J.: Experimental study of interactions of shock wave with free-stream turbulence. *J. Fluid Eng.* **{116}**, 763-769 (1994). <https://doi.org/10.1115/1.2911847>
28. Agui, J. H., Briassulis, G., Andreopoulos, Y.: Studies of interactions of a propagating shock wave with a

decaying grid turbulence: Velocity and vorticity fields. *J. Fluid Mech.* **{524}**, 143-195 (2005).

<https://doi.org/10.1017/S0022112004002514>

29. Xanthos, S., Briassulis, G., Andreopoulos, Y.: Interaction of decaying freestream turbulence with a moving shock wave: Pressure field: *J. Propul. Power* **{18}**, 1289-1297 (2002). <https://doi.org/10.2514/2.6066>
30. Tamba, T., Nguyen, T.M., Takeya, K., Harasaki, T., Iwakawa, A., Sasoh, A.: Counter-driver shock tube. *Shock Waves* **{25}**, 667-674 (2015). <https://doi.org/10.1007/s00193-015-0594-z>
31. Tamba, T., Fukushima, G., Kayumi, M., Iwakawa, A., Sasoh, A.: Experimental investigation of the interaction of a weak shock with grid turbulence in a counter-driver shock tube: *Phys. Rev. Fluids* **{4}**, 073401 (2019). <https://doi.org/10.1103/PhysRevFluids.4.073401>
32. Fukushima, G., Tamba, T., Iwakawa, A., Sasoh, A.: Influence of cellophane diaphragm rupture processes on the shock wave formation in a shock tube. *Shock Waves* (2020). <https://doi.org/10.1007/s00193-020-00951-2>
33. Britan, A., Igra, O., Ben-Dor, G., Shapiro, H.: Shock wave attenuation by grids and orifice plates. *Shock Waves* **{16}**, 1–15 (2006). <https://doi.org/10.1007/s00193-006-0019-0>
34. Roach, P. E.: The generation of nearly isotropic turbulence by means of grids, *Int. J. Heat Fluid Flow* **{8}**, 82-92 (1987). [https://doi.org/10.1016/0142-727X\(87\)90001-4](https://doi.org/10.1016/0142-727X(87)90001-4)
35. Kitamura, T., Nagata, K., Sakai, Y., Sasoh, A., Terashima, O., Saito, H., Harasaki, T.: On invariants in grid turbulence at moderate Reynolds numbers. *J. Fluid Mech.* **{738}**, 378-406 (2014). <https://doi.org/10.1017/jfm.2013.595>

36. Briassulis, G., Agui, J.H., Andreopoulos, Y.: The structure of weakly compressible grid-turbulence. *J. Fluid Mech.* **{432}**, 219-283 (2001). <https://doi.org/10.1017/S0022112000003402>
37. Tanaka, K., Watanabe, T., and Nagata, K.: Statistical analysis of deformation of a shock wave propagating in a local turbulent region. *Phys. Fluids* **{32}**, 096107 (2020). <https://doi.org/10.1063/5.0019784>